INORGANIC CHEMISTRY FRONTIERS

RESEARCH ARTICLE

View Article Online
View Journal | View Issue

Cite this: *Inorg. Chem. Front.*, 2026, **13**, 4309

Molecular pseudo-halogen engineering enables remarkable birefringence enhancement in hybrid perovskites

Yao Yao,[a,c,d] Yanqiang Li,*[a,b] Bin Chen,[a] Yipeng Song,[a,c,d] Weiqi Huang,[a,d] Zhiyong Bai,[a] Junhua Luo *[a,c,d,e] and Sangen Zhao *[b]

Hybrid perovskites have emerged as promising candidates for birefringent crystals due to their structural diversity. Conventional strategies to enhance birefringence often rely on incorporating highly π-conjugated organic components; however, it remains challenging to achieve both high birefringence (>0.3) and large single crystal growth. Herein, we present a pseudo-halogen engineering method that also enables giant birefringence enhancement. By substituting halogen Cl^- with polar pseudo-halogen $(SCN)^-$, we designed and synthesized a one-dimensional hybrid perovskite, namely $(C_6N_2H_{15})Cd(SCN)_3$, which exhibits a high birefringence of Δn_{exp} = 0.37@550 nm, more than 12 times that of isostructural $(C_6N_2H_{16})Cd_2Cl_6{\cdot}2H_2O$ (Δn_{exp} = 0.03@550 nm). This birefringence value not only surpasses those of all commercial birefringent crystals, but also is even higher than those of many hybrid perovskites composed of π-conjugated cations. Moreover, large single crystals of $(C_6N_2H_{15})Cd(SCN)_3$ were readily grown by the facile evaporation method. First-principles calculations reveal that the remarkable birefringence enhancement originates from a tens-of-times increase in polarizability anisotropy of the distorted $Cd(SCN)_6$ octahedra compared to their $CdCl_5{\cdot}H_2O$ counterparts. This work provides a novel molecular-level strategy towards designing high-performance birefringent crystals for polarized optics.

Received 24th December 2025,
Accepted 1st February 2026

DOI: 10.1039/d5qi02592c

rsc.li/frontiers-inorganic

1. Introduction

When light passes through an optically anisotropic crystal, it splits into two distinct rays, which are orthogonally polarized and travel at different speeds, namely, the ordinary and extraordinary rays.[1–3] This phenomenon enables birefringent crystals to modulate polarized light, making them indispensable in various polarized optical devices, such as polarizers, wave plates, mirrors, phase compensators, *etc.*[4–6] High birefringence is highly desirable, as it allows for the fabrication of more compact and efficient devices.[7–9] From the viewpoint of practical applications, it is also critical that large single crystals of these materials are easy to grow.[10] However, commercial birefringent crystals have long been limited to inorganic oxides and fluorides, which typically exhibit relatively small birefringence,[11–16] such as MgF_2 (0.011@532 nm),[11] $LiNbO_3$ (0.074@546 nm),[12] α-BaB_2O_4 (0.122@532 nm),[13] $CaCO_3$ (0.172@532 nm),[14] and YVO_4 (0.209@532 nm).[15] Moreover, it remains difficult to grow pure single crystals for some materials, like $CaCO_3$. These limitations have spurred the necessity to explore new birefringent crystals with superior comprehensive properties.

Recently, hybrid perovskites have emerged as promising candidates for birefringent crystals due to their rich structural diversity.[5,17–21] To enhance the birefringence, researchers have explored various strategies, one of which involves applying external thermal stimuli to induce structural phase transitions. However, the amplitude of birefringence enhancement by such physical means is relatively limited. For example, Sun *et al.* synthesized a two-dimensional (2D) tri-layered hybrid perovskite, namely $(CH_3NH_3)_2[(CH_3)_2CH(CH_2)_2NH_3]_2Pb_3Cl_{10}$, whose in-plane birefringence slightly improved from Δn_{exp} = 0 to Δn_{exp} = 0.01@546 nm upon cooling.[18]

It is widely acknowledged that macroscopic birefringence is strongly correlated with the polarizability anisotropy of crystal structures. On this basis, the other common effective strategies involve chemical modification, that is, introducing highly delocalized π-conjugated cations with inherent anisotropy of polarizability between the in-plane and out-of-plane directions.[17,21] In 2022, our group reported a new 2D layered hybrid perovskite, $(C_3N_6H_8)PbBr_4$, *via* the introduction of π-conjugated

[a]*State Key Laboratory of Functional Crystals and Devices, Fujian Institute of Research on the Structure of Matter, Chinese Academy of Sciences, Fuzhou 350002, P.R. China. E-mail: liyanqiang@quantumsc.cn*
[b]*Quantum Science Center of Guangdong-Hong Kong-Macao Greater Bay Area, Shenzhen 518045, P.R. China. E-mail: zhaosangen@quantumsc.cn*
[c]*University of the Chinese Academy of Sciences, Beijing 100049, P.R. China*
[d]*Fujian College, University of Chinese Academy of Sciences, Fuzhou 350002, P.R. China*
[e]*College of Chemistry, Fuzhou University, Fuzhou 350116, P. R. China. E-mail: jhluo@fjirsm.ac.cn*

organic cations $(C_3N_6H_8)^+$.[17] This birefringent crystal has a high birefringence of 0.322@550 nm, mainly attributed to π-conjugated $(C_3N_6H_8)^+$. Although such large π-conjugated cations can significantly enhance the birefringence, the resultant birefringent crystals are typically limited to micron-scale sizes, seriously hindering their practical applications.

In this work, by employing a non-π-conjugated, cheap organic component, *N*,*N*-dimethylpiperazine, we successfully synthesized and reported two novel hybrid perovskites, namely $(C_6N_2H_{16})Cd_2Cl_6{\cdot}2H_2O$ and $(C_6N_2H_{15})Cd(SCN)_3$, which feature similar 1D $[CdCl_3{\cdot}H_2O]_\infty$ and $[Cd(SCN)_3]_\infty$ perovskite chains, constructed by $CdCl_5{\cdot}H_2O$ and distorted $Cd(SCN)_6$ octahedra. Interestingly, there is a distinct birefringence gap between $(C_6N_2H_{16})Cd_2Cl_6{\cdot}2H_2O$ (Δn_{exp} = 0.03@550 nm) and $(C_6N_2H_{15})Cd(SCN)_3$ (Δn_{exp} = 0.37@550 nm), respectively. In other words, the birefringence has been improved by more than 12 times *via* the chemical substitution of halogen Cl^- ions with polar pseudo-halogen thiocyanide. The transparent crystal of $(C_6N_2H_{15})Cd(SCN)_3$ with dimensions up to 17 × 4 × 2 mm^3 has been successfully grown.

2. Results and discussion

Polycrystalline samples of $(C_6N_2H_{16})Cd_2Cl_6{\cdot}2H_2O$ and $(C_6N_2H_{15})Cd(SCN)_3$ were synthesized by the facile solution method. Large single crystals of $(C_6N_2H_{15})Cd(SCN)_3$ were successfully grown by slow evaporation from its solution (Fig. S1). Their phase purities were confirmed by powder X-ray diffraction (XRD) analysis, as demonstrated in Fig. S2, in which experimental patterns match well with the simulated ones. Besides, the powder XRD patterns of $(C_6N_2H_{15})Cd(SCN)_3$ remained highly consistent over time (Fig. S3) even after a month of air exposure, indicating that $(C_6N_2H_{15})Cd(SCN)_3$ has good air stability.

Single-crystal XRD analysis revealed that both $(C_6N_2H_{16})Cd_2Cl_6{\cdot}2H_2O$ and $(C_6N_2H_{15})Cd(SCN)_3$ crystallize in the monoclinic space group $P2_1/c$ (no. 14) (see detailed crystallographic information listed in Tables S1–S5). As shown in Fig. 1a and b, in both compounds, central Cd^{2+} ions exhibit similar octahedral coordination environments. In $(C_6N_2H_{16})Cd_2Cl_6{\cdot}2H_2O$,

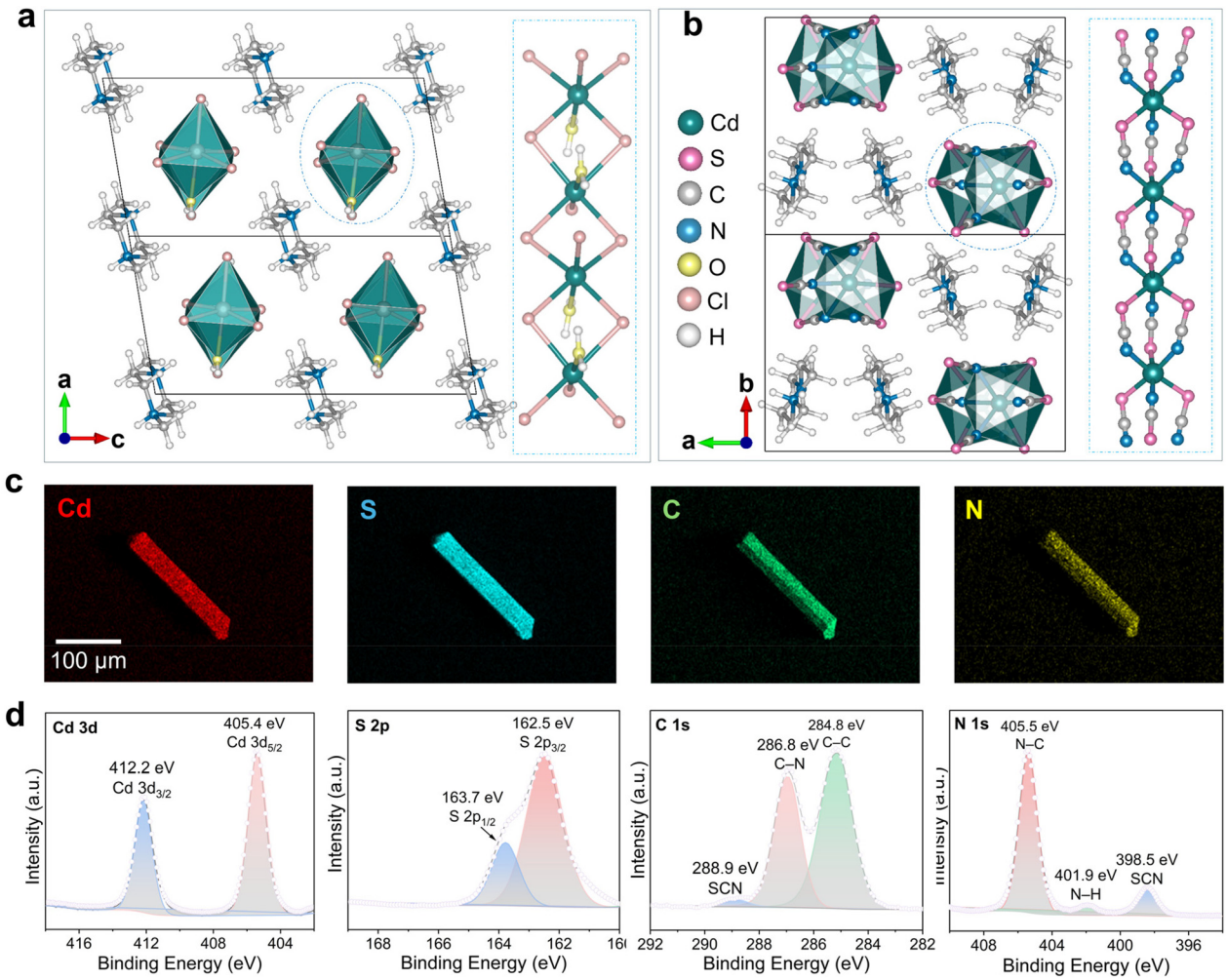

Fig. 1 Structural and compositional analyses of $(C_6N_2H_{16})Cd_2Cl_6{\cdot}2H_2O$ and $(C_6N_2H_{15})Cd(SCN)_3$. (a) The crystal structure of $(C_6N_2H_{16})Cd_2Cl_6{\cdot}2H_2O$ viewed along the *b*-axis. (b) The crystal structure of $(C_6N_2H_{15})Cd(SCN)_3$ viewed along the *c*-axis. (c) Scanning electron microscopy elemental mapping for $(C_6N_2H_{15})Cd(SCN)_3$. (d) XPS fine spectra for Cd 3d, S 2p, C 1s, and N 1s in $(C_6N_2H_{15})Cd(SCN)_3$.

each Cd^{2+} is coordinated by one H_2O and five Cl^-, forming $CdCl_5{\cdot}H_2O$ octahedra (Fig. S4), while in $(C_6N_2H_{15})Cd(SCN)_3$, six $(SCN)^-$ ligands coordinate with Cd^{2+} to form twisted $Cd(SCN)_6$ octahedra (Fig. S4). These octahedra are further interconnected with each other to construct similar 1D perovskite frameworks of $[Cd(SCN)_3]_\infty$ and $(CdCl_3{\cdot}H_2O)_\infty$ chains (Fig. 1a and b). The organic *N*,*N*-dimethylpiperazine cations reside between the infinite $(CdCl_3{\cdot}H_2O)_\infty$ and $[Cd(SCN)_3]_\infty$ chains, keeping the overall structural balance. In $(C_6N_2H_{16})Cd_2Cl_6{\cdot}2H_2O$, Cd–Cl bonds fall in the length range of 2.5640(6)–2.6622(6) Å, and Cd–O bond lengths are 2.4265(16) Å (Table S4). Similarly, in $(C_6N_2H_{15})Cd(SCN)_3$, Cd–S bond lengths fall in the range of 2.6453(6) Å to 2.8280(6) Å, and Cd–N bond distances vary between 2.2450(2) Å and 2.3636(19) Å (Table S4). In addition, $(SCN)^-$ ligands adopt an almost linear geometry with angles ranging from 177.9(2)° to 179.7(2)° (Table S5). According to previous reports, all these bond lengths and bond angles are reasonable.[22,23] Notably, in the crystal structure of $(C_6N_2H_{15})Cd(SCN)_3$, the $(SCN)^-$ ligands basically align along the *c*-axis, which means it should exhibit larger optical anisotropy along the *c* axis than that along the *a*-axis and *b*-axis. This structural arrangement is beneficial for large birefringence. Moreover, $[Cd(SCN)_3]_\infty$ chains realize basically an optimal parallel arrangement, further improving the overall birefringence performance of $(C_6N_2H_{15})Cd(SCN)_3$.

Energy dispersive X-ray spectroscopy mapping confirms the expected composition and uniform distribution within the crystal (Fig. 1c and Fig. S5 and 6). In addition, X-ray photoelectron spectroscopy (XPS) was further employed to investigate the chemical composition of $(C_6N_2H_{15})Cd(SCN)_3$ (Fig. S7 and Fig. 1d), in which C 1s, N 1s, S 2p, and Cd 3d signals were clearly observed. The fine XPS spectrum of Cd 3d exhibits two peaks at approximately 412.2 eV and 405.4 eV, which correspond to Cd $3d_{3/2}$ and Cd $3d_{5/2}$, respectively.[24] In the fine spectrum of S 2p, there are two major peaks at about 162.5 eV and 163.7 eV, coming from $2p_{3/2}$ and $2p_{1/2}$.[25] As for the C 1s spectrum, the peak at 284.8 eV belongs to C–C from the adventitious C. The other peaks at 286.8 eV and 288.9 eV derive from the C of the organic cation *N*,*N*-dimethylpiperazine and C of $(SCN)^-$.[25] The fine spectrum of N 1s contains three peaks at 398.5 eV, 401.9 eV, and 405.4 eV, in which the strongest peak at 405.4 eV is related to C–N. Other binding energies located at 398.5 eV and 401.9 eV are attributed to the N of $(SCN)^-$ and N–H bonding.[25] Fourier transform infrared spectroscopy (FTIR) and Raman spectroscopy of $(C_6N_2H_{16})Cd_2Cl_6{\cdot}2H_2O$ and $(C_6N_2H_{15})Cd(SCN)_3$ were conducted in the spectral range between 4000 and 400 cm^{-1} (Fig. S8 and S9). Some strong and sharp peaks corresponding to characteristic bending and stretching vibrations of the organic cation *N*,*N*-dimethylpiperazine could be observed. In addition, the sharp absorption signals at about 2098/2121 cm^{-1} in FTIR spectroscopy and 2099/2122 cm^{-1} in Raman spectroscopy correspond to vibrations of $(SCN)^-$.[26]

The thermal properties of $(C_6N_2H_{16})Cd_2Cl_6{\cdot}2H_2O$ and $(C_6N_2H_{15})Cd(SCN)_3$ were analyzed using differential thermal and thermogravimetric analyses (Fig. S10), which show that $(C_6N_2H_{15})Cd(SCN)_3$ remains thermally stable up to 519 K, whereas $(C_6N_2H_{16})Cd_2Cl_6{\cdot}2H_2O$ exhibits lower thermal stability of about 373 K. The UV-visible-near-infrared diffuse reflectance spectra of $(C_6N_2H_{16})Cd_2Cl_6{\cdot}2H_2O$ and $(C_6N_2H_{15})Cd(SCN)_3$ were recorded from 200 nm to 800 nm, respectively (Fig. S11). Based on the Kubelka–Munk function,[27] the calculated absorption data indicate that the bandgap of $(C_6N_2H_{16})Cd_2Cl_6{\cdot}2H_2O$ is about 4.38 eV, while that of $(C_6N_2H_{15})Cd(SCN)_3$ is about 3.69 eV.

To investigate the structural anisotropic characteristics of $(C_6N_2H_{15})Cd(SCN)_3$, angle-resolved polarized Raman spectroscopy (ARPRS) was performed, whose measurement schematic diagram is illustrated in Fig. 2a. The incident laser was initially polarized using the linear polarizer, while a half-wave plate was then introduced into the shared optical path to adjust the polarization directions. The intensity of Raman vibrations follows the relation:

$$I \propto |e_i \times R \times e_s|^2$$

where R is the Raman tensor, and e_i and e_s represent the unit polarization vectors of the incident and scattered signal, respectively. Given that $(C_6N_2H_{15})Cd(SCN)_3$ crystallizes in the monoclinic space group $P2_1/c$ (no. 14), only the A_g and B_g vibrational modes contribute to Raman activities. Their respective Raman tensors are expressed as:[28]

$$R(A_g) = \begin{bmatrix} b & 0 & d \\ 0 & c & 0 \\ d & 0 & a \end{bmatrix}$$

$$R(B_g) = \begin{bmatrix} 0 & f & 0 \\ f & 0 & e \\ 0 & e & 0 \end{bmatrix}$$

Accordingly, the intensities of Raman vibrations on the (010) plane in the parallel and perpendicular polarization configurations for $(C_6N_2H_{15})Cd(SCN)_3$ can be described by:[29]

$$I(A, \parallel) \propto d \sin 2\theta + (a-b)\sin^2\theta + b$$

$$I(B, \parallel) \propto 0$$

$$I(A, \perp) \propto 2d \cos 2\theta + (a-b)\sin 2\theta$$

$$I(B, \perp) \propto 0$$

Herein the θ denotes the angle between the *b*-axis and the polarization direction of the incident light.

Fig. 2b and c display the 2D false-color contour ARPRS maps of $(C_6N_2H_{15})Cd(SCN)_3$ under parallel and perpendicular polarization configurations, as rotation angles change from 0° to 360°. The observed periodic changes of Raman vibrations reflect the strongly anisotropic nature of molecular vibrations in $(C_6N_2H_{15})Cd(SCN)_3$. Fig. 2d and e depict the polar plots showing polarization-resolved intensity variation of the Raman mode intensity at 2096 cm^{-1}. In both polarization configurations, this peak exhibits a characteristic two-lobed shape, agreeing well with the theoretical expressions.

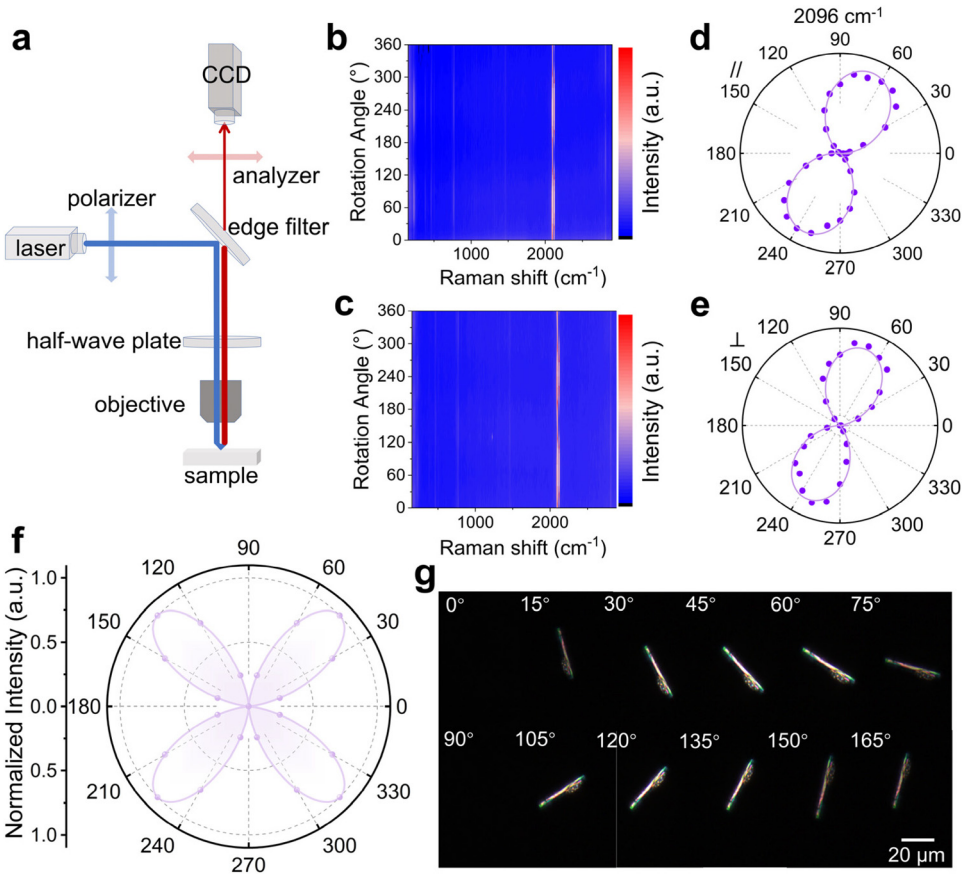

Fig. 2 The anisotropic investigation of $(C_6N_2H_{15})Cd(SCN)_3$. (a) The schematic diagram of ARPRS measurement. 2D contour color maps of polarized Raman intensity under (b) parallel- and (c) perpendicular-polarization configurations for $(C_6N_2H_{15})Cd(SCN)_3$. The polar plots showing polarized Raman intensity at 2096 cm^{-1} under (d) parallel- and (e) perpendicular-polarization configurations for $(C_6N_2H_{15})Cd(SCN)_3$. (f) The normalized fitted polar plots showing the relationship between the transmitted light intensity and the rotation angle. (g) Transmitted images under cross polarized light in increments of 15° from 0° to 165° for $(C_6N_2H_{15})Cd(SCN)_3$.

To reveal the anisotropic optical behavior of $(C_6N_2H_{16})Cd_2Cl_6{\cdot}2H_2O$ and $(C_6N_2H_{15})Cd(SCN)_3$, we further carried out polarization-resolved optical microscopy measurement. As shown in Fig. 2g and Fig. S12, the brightness changes periodically every 45° with the rotation of both tested single crystals. This phenomenon is consistent with the normalized fitted polar plots showing the relationship between the transmitted light intensity and the rotation angle (Fig. 2f), which clearly displays the in-plane optical anisotropy for the refraction of both structures.

The schematic diagram of the orthogonally polarized microscope is illustrated in Fig. 3a. When a beam of light passes through an optically anisotropic crystal along the non-optical-axis direction, it splits into two orthogonally polarized beams: the ordinary ray (o-ray) and the extraordinary ray (e-ray). These two beams exhibit different refractive indices due to the crystal's anisotropy, thereby generating birefringence. As shown in Fig. 3b and e, the original interference color of $(C_6N_2H_{16})Cd_2Cl_6{\cdot}2H_2O$ and $(C_6N_2H_{15})Cd(SCN)_3$ is first-order blue and third-order pink under the orthogonally polarized light, respectively, corresponding to the optical path difference of 0.60 μm and 1.54 μm. Both the measured single crystals could achieve complete extinction by using a Berek compensator when rotated clockwise and counterclockwise (Fig. 3c, d, f, and g). The thicknesses for the tested single crystals are 21.1 μm for $(C_6N_2H_{16})Cd_2Cl_6{\cdot}2H_2O$ and 4.3 μm for $(C_6N_2H_{15})Cd(SCN)_3$ (Fig. S13). Based on the single-crystal XRD analyses, the measured samples correspond to the (10−2) plane for $(C_6N_2H_{16})Cd_2Cl_6{\cdot}2H_2O$ (Fig. S14a) and the (010) crystal plane for $(C_6N_2H_{15})Cd(SCN)_3$ (Fig. S14b), which are the only natural crystal planes suitable for measurement. Therefore, according to the birefringence calculation formula provided in the SI,[30] the observed birefringence values were determined to be about $\Delta n_{(10-2)exp}$ = 0.03@550 nm for $(C_6N_2H_{16})Cd_2Cl_6{\cdot}2H_2O$ and about $\Delta n_{(010)exp}$ = 0.37@550 nm for $(C_6N_2H_{15})Cd(SCN)_3$.

The wavelength-dependent refractive indices at angles from 0° to 360° for the tested (10−2) and (010) crystal planes of $(C_6N_2H_{16})Cd_2Cl_6{\cdot}2H_2O$ and $(C_6N_2H_{15})Cd(SCN)_3$ were obtained and are shown in Fig. S15. The changes in refractive indices at λ = 550 nm are further presented in polar plots (Fig. 3h and k). From the ellipsoidal fitting drawn with the solid line, the

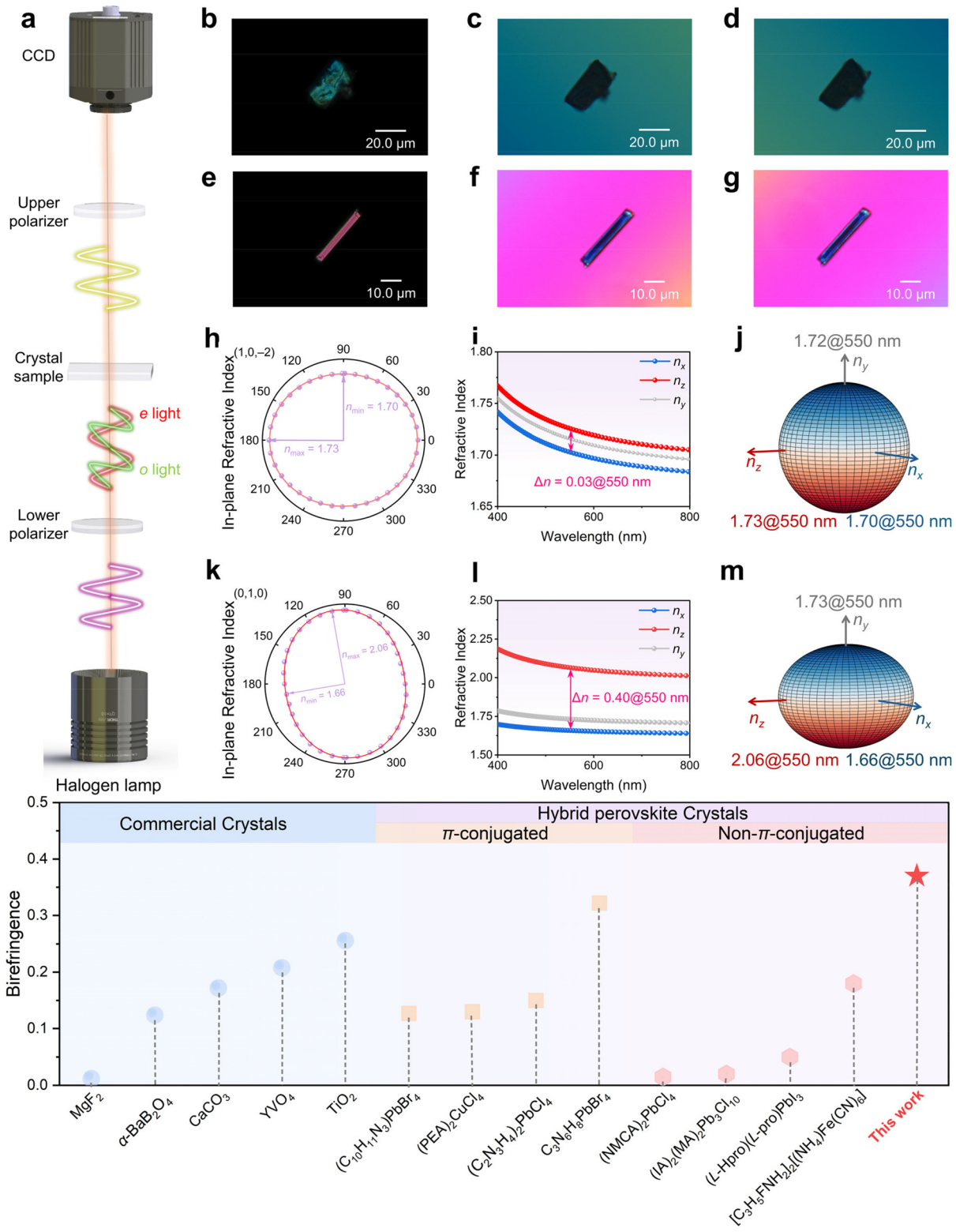

Fig. 3 Birefringence properties of $(C_6N_2H_{16})Cd_2Cl_6{\cdot}2H_2O$ and $(C_6N_2H_{15})Cd(SCN)_3$. (a) Schematic diagram of the polarized microscopy method. Original interference color of the crystal sample under the orthogonally polarized light of (b) $(C_6N_2H_{16})Cd_2Cl_6{\cdot}2H_2O$ and (e) $(C_6N_2H_{15})Cd(SCN)_3$. Complete extinction of (c and d) $(C_6N_2H_{16})Cd_2Cl_6{\cdot}2H_2O$ and (f and g) $(C_6N_2H_{15})Cd(SCN)_3$ achieved by clockwise and counterclockwise rotation of the compensator. Polar plots of calculated refractive indices at λ = 550 nm in different directions for the (10−2) plane of $(C_6N_2H_{16})Cd_2Cl_6{\cdot}2H_2O$ (h) and the (010) plane of $(C_6N_2H_{15})Cd(SCN)_3$ (k). The solid lines are fit to guide the eyes. Theoretically calculated refractive indices and birefringence of (i) $(C_6N_2H_{16})Cd_2Cl_6{\cdot}2H_2O$ and (l) $(C_6N_2H_{15})Cd(SCN)_3$. Triaxial ellipsoid of three principal refractive indices of (j) $(C_6N_2H_{16})Cd_2Cl_6{\cdot}2H_2O$ and (m) $(C_6N_2H_{15})Cd(SCN)_3$ at λ = 550 nm. (n) Comparison of the birefringence of $(C_6N_2H_{15})Cd(SCN)_3$ with that of representative commercial birefringent crystals and some reported hybrid perovskite birefringent crystals.

maximum refractive index and minimum refractive index at λ = 550 nm were determined. The calculated birefringence values for the (10−2) plane of $(C_6N_2H_{16})Cd_2Cl_6{\cdot}2H_2O$ and the (010) plane of $(C_6N_2H_{15})Cd(SCN)_3$ are $\Delta n_{(10-2)cal}$ = 0.03@550 nm and $\Delta n_{(010)cal}$ = 0.40@550 nm, which match well with the experimental results, $\Delta n_{(10-2)exp}$ = 0.03@550 nm and $\Delta n_{(010)exp}$ = 0.37@550 nm. Considering that both $(C_6N_2H_{16})Cd_2Cl_6{\cdot}2H_2O$ and $(C_6N_2H_{15})Cd(SCN)_3$ crystallize in the monoclinic space

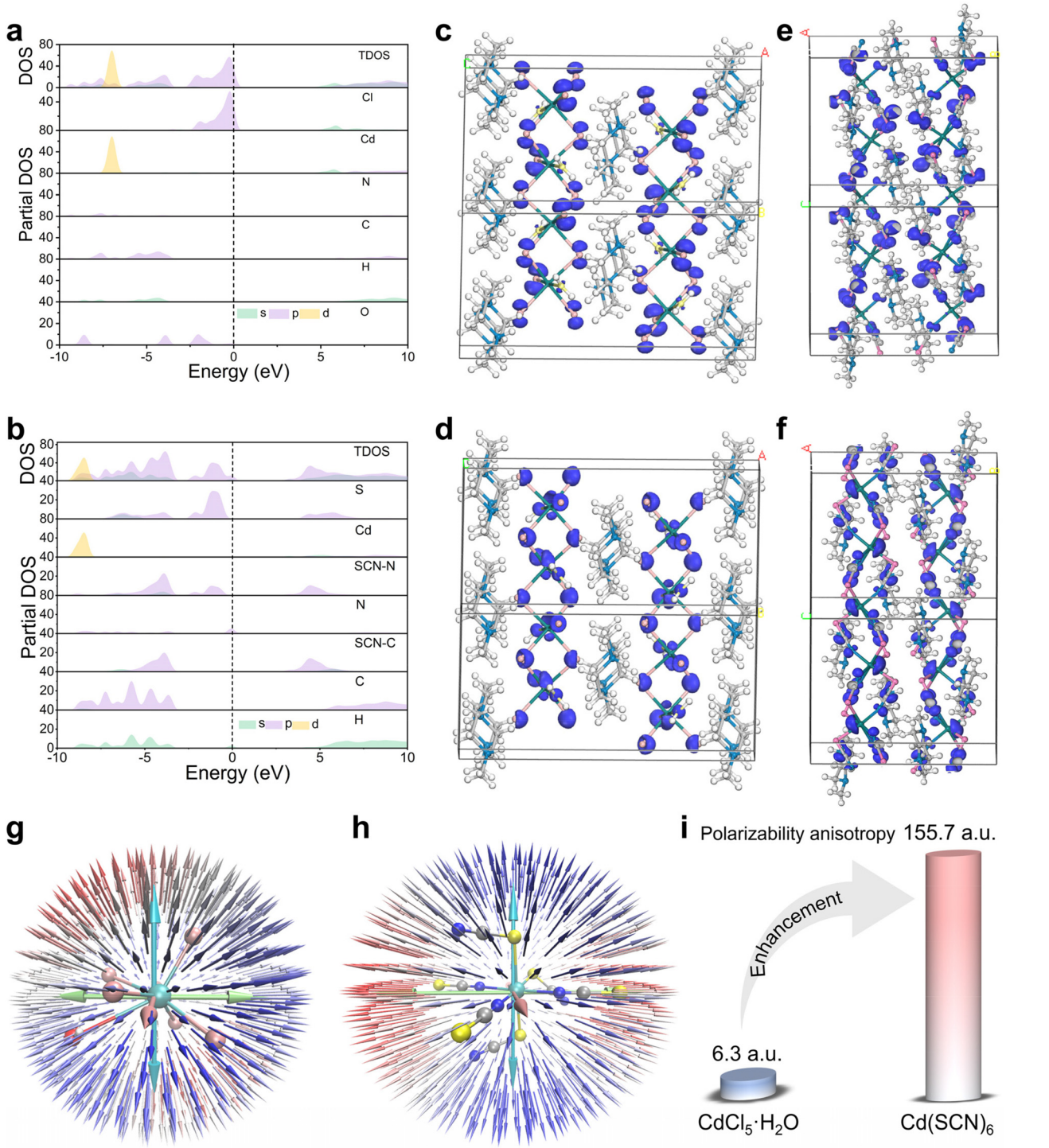

Fig. 4 Theoretical calculations of $(C_6N_2H_{16})Cd_2Cl_6{\cdot}2H_2O$ and $(C_6N_2H_{15})Cd(SCN)_3$. Total and partial DOS of (a) $(C_6N_2H_{16})Cd_2Cl_6{\cdot}2H_2O$ and (b) $(C_6N_2H_{15})Cd(SCN)_3$. The HOMO of (c) $(C_6N_2H_{16})Cd_2Cl_6{\cdot}2H_2O$ and (e) $(C_6N_2H_{15})Cd(SCN)_3$. The LUMO of (d) $(C_6N_2H_{16})Cd_2Cl_6{\cdot}2H_2O$ and (f) $(C_6N_2H_{15})Cd(SCN)_3$. The unit sphere representation map of the polarizability tensor of (g) $CdCl_5{\cdot}H_2O$ and (h) $Cd(SCN)_6$. (i) The comparison of the polarizability anisotropy between $CdCl_5{\cdot}H_2O$ and $Cd(SCN)_6$.

group $P2_1/c$ (no. 14), one of their three principal optical axes aligns with the crystallographic *b*-axis, while the other two are located within the (010) crystal plane. As demonstrated in Fig. 3i and l, the overall birefringence of $(C_6N_2H_{16})Cd_2Cl_6{\cdot}2H_2O$ and $(C_6N_2H_{15})Cd(SCN)_3$ is calculated to be about Δn_{cal} = 0.03@550 nm and 0.40@550 nm. In addition, the triaxial ellipsoid corresponding to the three principal refractive indices at λ = 550 nm also exhibits significant difference in optical anisotropy (Fig. 3j and m). Clearly, compared to $(C_6N_2H_{16})Cd_2Cl_6{\cdot}2H_2O$, the birefringence of $(C_6N_2H_{15})Cd(SCN)_3$ has increased more than 12 times by the chemical substitution of halogen Cl^- ions with pseudo-halogen $(SCN)^-$. Remarkably, the birefringence of $(C_6N_2H_{15})Cd(SCN)_3$ represents almost the largest value among reported hybrid perovskites without π-conjugated cations, exceeding that of recently reported $(IA)_2(MA)_2Pb_3Cl_{10}$,[18] (L-Hpro)(L-pro)PbI_3,[31] $(NMCA)_2PbCl_4$,[32] and $[C_3H_5FNH_2]_2[(NH_4)Fe(CN)_6]$.[33] Furthermore, it is also comparable to those of numerous hybrid perovskite birefringent crystals containing π-conjugated cations, including $(C_{10}H_{11}N_3)PbBr_4$,[34] $C_3N_6H_8PbBr_4$,[17] $(PEA)_2CuCl_4$,[5] and $(C_2N_3H_4)_2PbCl_4$.[19]

To understand the significant difference in birefringence between $(C_6N_2H_{16})Cd_2Cl_6{\cdot}2H_2O$ and $(C_6N_2H_{15})Cd(SCN)_3$, the first-principles calculations were performed by using the CASTEP package based on density functional theory.[35,36] Electronic band structure analyses reveal that $(C_6N_2H_{16})Cd_2Cl_6{\cdot}2H_2O$ features an indirect band gap of 4.58 eV (Fig. S16a), while $(C_6N_2H_{15})Cd(SCN)_3$ has a direct band gap of 3.58 eV (Fig. S16b), both of which align well with the experimental result (4.38 eV and 3.69 eV). Fig. 4a and b show the total and partial density of states (DOS) of $(C_6N_2H_{16})Cd_2Cl_6{\cdot}2H_2O$ and $(C_6N_2H_{15})Cd(SCN)_3$. For $(C_6N_2H_{16})Cd_2Cl_6{\cdot}2H_2O$, the upper valence bands near the Fermi level are mainly derived from Cl 3p orbitals and the bottom of conduction bands predominantly consists of Cd 5s orbitals, suggesting that $CdCl_5{\cdot}H_2O$ polyhedra significantly influence the optical properties of $(C_6N_2H_{16})Cd_2Cl_6{\cdot}2H_2O$, while the contribution from the *N*,*N*-dimethylpiperazine cations remains minimal. In contrast, for $(C_6N_2H_{15})Cd(SCN)_3$, the upper valence bands near the Fermi level are predominantly composed of S 2p orbitals and SCN-N 2p orbitals. The bottom of conduction bands is mainly contributed by SCN-N 2p orbitals, SCN-C 2p orbitals, and S 2p orbitals together with a small amount of Cd 5s orbitals. This indicates that $Cd(SCN)_6$ polyhedra play a dominant role in the optical properties of $(C_6N_2H_{15})Cd(SCN)_3$, while the contribution from the *N*,*N*-dimethylpiperazine cations is negligible. To further elucidate these contributions, the highest occupied molecular orbitals (HOMO) and the lowest unoccupied molecular orbitals (LUMO) were also calculated. Fig. 4c and d demonstrate that the HOMO and LUMO for $(C_6N_2H_{16})Cd_2Cl_6{\cdot}2H_2O$ are mainly influenced by Cl 3p orbitals, O 2p orbitals, and Cd 5s orbitals. As presented in Fig. 4e and f, the HOMO of $(C_6N_2H_{15})Cd(SCN)_3$ is mainly occupied by SCN-N 2p orbitals and S 2p orbitals, while the LUMO consists of SCN-N 2p orbitals, SCN-C 2p orbitals, and Cd 5s orbitals.

Despite both $CdCl_5{\cdot}H_2O$ and $Cd(SCN)_6$ adopting similar octahedral configurations, why does $(C_6N_2H_{15})Cd(SCN)_3$ exhibit much larger birefringence than $(C_6N_2H_{16})Cd_2Cl_6{\cdot}2H_2O$? Since macroscopic birefringence is closely related to the microscopic polarizability of functional groups, we calculated the polarizability tensors of $CdCl_5{\cdot}H_2O$ and $Cd(SCN)_6$ octahedra.[37,38] As demonstrated in Table S6, the polarizability tensor of $CdCl_5{\cdot}H_2O$ remains almost the same along different directions with α_{xx} = 210.1 a.u., α_{yy} = 212.5 a.u., and α_{zz} = 207.1 a.u. In contrast, in $Cd(SCN)_6$, the components of the polarizability tensor aligned with the polar $(SCN)^-$ chain direction (α_{xx} = 536.1 a.u.) are significantly larger than those of other directions (α_{yy} = 399.7 a.u. and α_{zz} = 372.3 a.u.). In order to further visualize these differences, we plotted the unit sphere representation map of $CdCl_5{\cdot}H_2O$ and $Cd(SCN)_6$ polyhedra.[37–39] As shown in Fig. 4g and h, the lengths of large bidirectional arrows represent the total magnitude of polarizability along the *X*, *Y*, and *Z* directions, while the small arrows indicate the changes in dipole moment induced by an external electric field applied from the molecular center. The nearly spherical distribution for $CdCl_5{\cdot}H_2O$ reflects its isotropic polarizability nature. In contrast, the polarizability tensor of $Cd(SCN)_6$ along the polar $(SCN)^-$ chain direction is significantly larger than those along other directions, indicating pronounced polarizability anisotropy. Quantitatively, the polarizability anisotropy ($\Delta\alpha$) of $Cd(SCN)_6$ reaches 155.7 a.u., which is considerably larger than that of $CdCl_5{\cdot}H_2O$ ($\Delta\alpha$ = 6.3 a.u.) (Fig. 4i). Moreover, the 1D $Cd(SCN)_3$ chains are arranged in parallel within the crystal structure of $(C_6N_2H_{15})Cd(SCN)_3$, which facilitates the effective superposition of polarizability anisotropy, further inducing large optical birefringence of $(C_6N_2H_{15})Cd(SCN)_3$.

3. Conclusions

In summary, we present a polar pseudo-halogen substitution strategy that significantly enhances the birefringence of hybrid perovskites by over an order of magnitude—from 0.03@550 nm for $(C_6N_2H_{16})Cd_2Cl_6{\cdot}2H_2O$ to 0.37@550 nm for isostructural $(C_6N_2H_{15})Cd(SCN)_3$. Theoretical calculations and structural analyses confirm that the pronounced birefringence gap arises from the substantial increase in polarizability anisotropy induced by replacing halide Cl^- ions with pseudo-halogen $(SCN)^-$. Such a birefringence value of $(C_6N_2H_{15})Cd(SCN)_3$ exceeds those of all commercial birefringent crystals and ranks almost the highest among those for reported hybrid perovskites with non-π-conjugated organic cations. Combining the outstanding birefringence performance and ease of growth of large single-crystals of $(C_6N_2H_{15})Cd(SCN)_3$, this work establishes a scalable chemical design paradigm for developing outstanding birefringent crystals in the future.

Author contributions

All authors have given approval to the final version of the manuscript.

Conflicts of interest

The authors declare no competing financial interest.

Data availability

Experimental and characterization details are given in the article and supplementary information (SI). The Supplementary Information includes Experimental Section, XPS Analysis, Powder XRD, FTIR, Raman, Angle-resolved Polarized Raman, UV-Vis-NIR Diffuse Reflectance Spectroscopy, Birefringence Tests, Theoretical Calculations. See DOI: https://doi.org/10.1039/d5qi02592c.

CCDC 2467217 ($(C_6N_2H_{15})Cd(SCN)_3$) and 2467218 ($(C_6N_2H_{16})Cd_2Cl_6{\cdot}2H_2O$) contain the supplementary crystallographic data for this paper.[40a,b]

Acknowledgements

The authors of this work acknowledge the financial support from the National Natural Science Foundation of China (22405273 and 22193042), the Young Elite Scientists Sponsorship Program by CAST (YESS20230117 and YESS20240439), the Natural Science Foundation of Fujian Province (2022J02012), and the Key Research Program of Frontier Sciences of the Chinese Academy of Sciences (ZDBS-LY-SLH024).

References

1 S. Y. Niu, G. Joe, H. Zhao, Y. C. Zhou, T. Orvis, H. X. Huyan, J. Salman, K. Mahalingam, B. Urwin, J. B. Wu, Y. Liu, T. E. Tiwald, S. B. Cronin, B. M. Howe, M. Mecklenburg, R. Haiges, D. J. Singh, H. Wang, M. A. Kats and J. Ravichandran, Giant optical anisotropy in a quasi-one-dimensional crystal, *Nat. Photonics*, 2018, **12**, 392–393.

2 Y. Zhou, Z. F. Guo, H. G. Gu, Y. Q. Li, Y. P. Song, S. Y. Liu, M. C. Hong, S. E. Zhao and J. H. Luo, A solution-processable natural crystal with giant optical anisotropy for efficient manipulation of light polarization, *Nat. Photonics*, 2024, **18**, 922–927.

3 Q. Guo, Q. Zhang, T. Zhang, J. Zhou, S. Xiao, S. Wang, Y. P. Feng and C. W. Qiu, Colossal in-plane optical anisotropy in a two-dimensional van der Waals crystal, *Nat. Photonics*, 2024, **18**, 1170–1175.

4 X. M. Chen, W. G. Lu, J. L. Tang, Y. Y. Zhang, Y. T. Wang, G. D. Scholes and H. Z. Zhong, Solution-processed inorganic perovskite crystals as achromatic quarter-wave plates, *Nat. Photonics*, 2021, **15**, 813–816.

5 Y. Dou, M. S. Tumusange, J. Jin, X. Wang, E. R. Crater, S. Liu, L. Zhu, S. Zuberi, G. Harman, C. Weaver, B. Ramanujam, A. Shan, R. B. Moore, N. J. Podraza, Y. Yan and L. Quan, Broadband Achromatic Quarter-Waveplate Using 2D Hybrid Copper Halide Single Crystals, *J. Am. Chem. Soc.*, 2023, **145**, 18007–18014.

6 Z. Bai and K. M. Ok, Designing Sulfate Crystals with Strong Optical Anisotropy through π-Conjugated Tailoring, *Angew. Chem., Int. Ed.*, 2024, **63**, e202315311.

7 Y. Q. Li, X. Zhang, Y. Zhou, W. Q. Huang, Y. P. Song, H. Wang, M. J. Li, M. C. Hong, J. H. Luo and S. G. Zhao, An optically anisotropic crystal with large birefringence arising from cooperative π orbitals, *Angew. Chem., Int. Ed.*, 2022, **61**, e202208811.

8 Y. Li and K. M. Ok, Breaking Boundaries: Giant Ultraviolet Birefringence in Dimension-Reduced Zn-Based Crystals, *Angew. Chem., Int. Ed.*, 2024, **63**, e202409336.

9 W. Chen, B. Zhang, K. Tao, Q. Li, J. L. Sun and Q. Yan, Giant *ab*-Plane Birefringence in Quasi-1D Fibrous Red Phosphorus, *Angew. Chem., Int. Ed.*, 2024, **63**, e202403531.

10 T. Tong, W. Zhang, Z. Yang and S. Pan, Series of Crystals with Giant Optical Anisotropy: A Targeted Strategic Research, *Angew. Chem., Int. Ed.*, 2021, **60**, 1332–1338.

11 M. J. Dodge, Refractive properties of magnesium fluoride, *Appl. Opt.*, 1984, **23**, 1980–1985.

12 D. E. Zelmon, D. L. Small and D. Jundt, Infrared corrected Sellmeier coefficients for congruently grown lithium niobate and 5 mol% magnesium oxide-doped lithium niobate, *J. Opt. Soc. Am. B*, 1997, **14**, 3319–3322.

13 G. Q. Zhou, J. Xu, X. D. Chen, H. Y. Zhong, S. T. Wang, K. Xu, P. Z. Deng and F. X. Gan, Growth and spectrum of a novel birefringent α-BaB_2O_4 crystal, *J. Cryst. Growth*, 1998, **191**, 517–519.

14 G. Ghosh, Dispersion-equation coefficients for the refractive index and birefringence of calcite and quartz crystals, *Opt. Commun.*, 1999, **163**, 95–102.

15 L. G. DeShazer, Improved mid-infrared polarizers using yttrium vanadate, *Proc. SPIE*, 2002, **4481**, 10–16.

16 J. R. DeVore, Refractive indices of rutile and sphalerite, *J. Opt. Soc. Am. A*, 1951, **41**, 416–419.

17 W. Huang, X. Zhang, Y. Li, Y. Zhou, X. Chen, X. Li, F. Wu, M. Hong, J. Luo and S. Zhao, A hybrid halide perovskite birefringent crystal, *Angew. Chem., Int. Ed.*, 2022, **61**, e202202746.

18 J. Wang, Y. Ma, Z. Wang, X. Liu, S. Han, Y. Liu, W. Guo, J. Luo and Z. Sun, Unusual ferroelectric-dependent birefringence in 2D trilayered perovskite-type ferroelectric exploited by dimensional tailoring, *Matter*, 2022, **5**, 194–205.

19 Z. Wang, X. Chen, Y. Song, Z. Du, Y. Zhou, M. Li, W. Huang, Q. Xu, Y. Li, S. Zhao and J. Luo, A Two-Dimensional Hybrid Perovskite with Heat Switching Birefringence, *Angew. Chem., Int. Ed.*, 2023, **62**, e202311086.

20 H. H. Chen, X. G. Chen, Z. K. Xu, H. Peng, Y. Qin, H. P. Lv, X. J. Song, S. Q. Hu, L. Y. Ji, J. S. Zhou, R. G. Xiong and W. Q. Liao, A 3D Hybrid Perovskite Ferroelastic with Triclinic-to-Cubic Phase Transition Boosts Temperature/Pressure Dual On/Off Switchable Birefringence, *Angew. Chem., Int. Ed.*, 2025, e202503681.

21 Q. Xu, Z. Wang, Y. Zhou, W. Huang, Y. Song, J. Zheng, Y. Li, L. Hou, J. Luo and S. Zhao, A Highly Optical Anisotropic Hybrid Metal Halide for Modulation and Generation of Polarized Light, *Adv. Funct. Mater.*, 2025, **35**, 2417431.

22 Z. X. Wang, Y. Zhang, Y. Y. Tang, P. F. Li and R. G. Xiong, Fluoridation Achieved Antiperovskite Molecular Ferroelectric in $[(CH_3)_2(F\text{-}CH_2CH_2)NH]_3(CdCl_3)(CdCl_4)$, *J. Am. Chem. Soc.*, 2019, **141**, 4372–4378.

23 S. Y. Zhang, X. Shu, Y. Zeng, Q. Y. Liu, Z. Y. Du, C. T. He, W. X. Zhang and X. M. Chen, Molecule-based nonlinear optical switch with highly tunable on-off temperature using a dual solid solution approach, *Nat. Commun.*, 2020, **11**, 2752.

24 V. G. Bhide, S. Salkalachen, A. C. Rastog, C. N. R. Rao and M. S. Hegde, Depth profile composition studies of thin film CdS:Cu_2S solar cells using XPS and AES, *J. Phys. D: Appl. Phys.*, 1981, **14**, 1647.

25 C. Wechwithayakhlung, D. M. Packwood, J. Chaopaknam, P. Worakajit, S. Ittisanronnachai, N. Chanlek, V. Promarak, K. Kongpatpanich, D. J. Harding and P. Pattanasattayavong, Tin(II) thiocyanate $Sn(NCS)_2$ - a wide band gap coordination polymer semiconductor with a 2D structure, *J. Mater. Chem. C*, 2019, **7**, 3452–3462.

26 H. Zhang, X. Wang, H. Zhu, W. Xiao and B. K. Teo, Synthesis and Structure of $[(12C4)_2Cd][Cd_2(SCN)_6]$. Formation of a Novel Tetragonal Net of Anionic Layered Structure of $[Cd_2(SCN)_6^{2-}]_\infty$ Templated by the Square-Shaped Sandwich $[(12C4)_2Cd]^{2+}$ Cation, *J. Am. Chem. Soc.*, 1997, **119**, 5463–5464.

27 J. Tauc, Absorption edge and internal electric fields in amorphous semiconductors, *Mater. Res. Bull.*, 1970, **5**, 721–729.

28 V. N. Denisov, B. N. Mavrin and V. B. Podobedov, Hyper-Raman scattering by vibrational excitations in crystals, glasses and liquids, *Phys. Rep.*, 1987, **151**, 1–92.

29 X. L. Liu, X. Zhang, M. L. Lin and P. H. Tan, Different angle-resolved polarization configurations of Raman spectroscopy: A case on the basal and edge plane of two-dimensional materials, *Chin. Phys. B*, 2017, **26**, 067802.

30 B. E. Sorensen, A revised Michel-Levy interference colour chart based on first-principles calculations, *Eur. J. Mineral.*, 2013, **25**, 5–10.

31 J. Cheng, G. Yi, Z. Zhang, Y. Long, H. Zeng, L. Huang, G. Zou and Z. J. A. C. Lin, In Situ Chiral Template Approach to Synthesize Homochiral Lead Iodides for Second-Harmonic Generation, *Angew. Chem.*, 2024, **136**, e202318385.

32 Y. Ma, B. Wang, W. Li, Y. Liu, W. Guo, H. Xu, L. Tang, Q. Fan, J. Luo and Z. Sun, Unusual Triple-State Switching of Thermally Induced Birefringence in a Two-Dimensional Perovskite Ferroelectric, *J. Am. Chem. Soc.*, 2024, **146**, 27287–27292.

33 H. Qiu, R. An, C. Cui, Z. Li, J. Yang, X. Wang, X. Hou, J. Li, J. Lu, J. Sun, Z. Yang, S. Pan and M. Mutailipu, Bridging the Interlayer Binding to Ordered π-Conjugated Units for Constructing High-Performing Light Polarization Crystals, *Angew. Chem., Int. Ed.*, 2025, e202507171.

34 L. L. Zhang, Q. Ding, P. Wang, Y. Zhang, Q. Y. Liu, Y. L. Wang and J. Luo, Achieving strong second harmonic generation effects induced via dimensional increase of PbX_6 octahedra and halogen substitutes in $(C_{10}H_{11}N_3)PbX_4$ (X = Cl or Br), *Inorg. Chem. Front.*, 2024, **11**, 3618–3625.

35 J. P. Perdew, K. Burke and M. Ernzerhof, Generalized gradient approximation made simple, *Phys. Rev. Lett.*, 1996, **77**, 3865–3868.

36 S. J. Clark, M. D. Segall, C. J. Pickard, P. J. Hasnip, M. J. Probert, K. Refson and M. C. Payne, First principles methods using CASTEP, *Z. Kristallogr.*, 2005, **220**, 567–570.

37 T. Lu and F. Chen, Multiwfn: A multifunctional wavefunction analyzer, *J. Comput. Chem.*, 2012, **33**, 580–592.

38 M. J. Frisch, G. W. Trucks, H. B. Schlegel, G. E. Scuseria, M. A. Robb, J. R. Cheeseman, G. Scalmani, V. Barone, G. A. Petersson, H. Nakatsuji, X. Li, M. Caricato, A. V. Marenich, J. Bloino, B. G. Janesko, R. Gomperts, B. Mennucci, H. P. Hratchian, J. V. Ortiz, A. F. Izmaylov, J. L. Sonnenberg, D. Williams-Young, F. Ding, F. Lipparini, F. Egidi, J. Goings, B. Peng, A. Petrone, T. Henderson, D. Ranasinghe, V. G. Zakrzewski, J. Gao, N. Rega, G. Zheng, W. Liang, M. Hada, M. Ehara, K. Toyota, R. Fukuda, J. Hasegawa, M. Ishida, T. Nakajima, Y. Honda, O. Kitao, H. Nakai, T. Vreven, K. Throssell, J. A. Montgomery Jr, J. E. Peralta, F. Ogliaro, M. J. Bearpark, J. J. Heyd, E. N. Brothers, K. N. Kudin, V. N. Staroverov, T. A. Keith, R. Kobayashi, J. Normand, K. Raghavachari, A. P. Rendell, J. C. Burant, S. S. Iyengar, J. Tomasi, M. Cossi, J. M. Millam, M. Klene, C. Adamo, R. Cammi, J. W. Ochterski, R. L. Martin, K. Morokuma, O. Farkas, J. B. Foresman and D. J. Fox, *Gaussian 16 Rev. B.01*, Wallingford, CT, 2016.

39 W. Humphrey, A. Dalke and K. Schulten, VMD: visual molecular dynamics, *J. Mol. Graphics*, 1996, **14**, 33–38.

40 (*a*) CCDC 2467217: Experimental Crystal Structure Determination, 2026, DOI: **10.5517/ccdc.csd.cc2ntbnh**; (*b*) CCDC 2467218: Experimental Crystal Structure Determination, 2026, DOI: **10.5517/ccdc.csd.cc2ntbpj**.